LASER & PHOTONICS REVIEWS
www.lpr-journal.org

Counterintuitive Reversal of Circular Dichroism via Controllable Plasmonic Guided Mode Resonance in Diatomic Metasurfaces

Jiaqi Cheng, Zhancheng Li, Duk-Yong Choi, Wenwei Liu, Yuebian Zhang, Shiwang Yu, Hua Cheng,* Jianguo Tian, and Shuqi Chen**

Chiral metasurfaces, featuring customizable chiroptical response, have shown great potential across diverse applications, including optical sensing, chiral emission, and light spin detection. However, most previous studies have focused on chiroptical response stemming from the resonance of nanoresonators or their coupling. Here, the great capability of controlling nonlocal resonance for achieving versatile manipulation of circular dichroism (CD) is demonstrated. A counterintuitive sign reversal of CD is realized by modulating the collective interference of the plasmonic guided mode resonances (GMRs) within diatomic metasurfaces. The designed metasurfaces, composed of two nanoresonators, can effectively couple both orthogonal linear-polarized components of circularly polarized light to the same GMR. Through a simple adjustment of the spacing of nanoresonators to modulate the interference between GMRs, continuous variation and sign reversal of CD are achieved. Importantly, due to the fact that the modulation of GMRs does not impact the chiral resonant modes of the nanoresonators, the significant advantages of the designed metasurfaces in achieving chiral optical encryption are experimentally demonstrated. This work introduces an effective approach for the continuous manipulation of CD without altering the structural geometric chirality. It provides novel insights into exploring chiroptical mechanisms and holds promise for applications in chiral sensing and light spin detection.

1. Introduction

Chirality, which describes objects that cannot be superposed onto their mirror images, is ubiquitous in natural materials. It plays a pivotal role in various critical areas, including life science, drug synthesis, analytical chemistry, and quantum optics.[1–4] The interaction between circularly polarized light and chiral materials gives rise to chiroptical responses, such as circular dichroism (CD) and circular birefringence.[5] These responses have been widely employed for detecting and discriminating the chirality of natural materials. However, the chiroptical responses in natural materials are limited by the mismatch between the small size of natural molecules and the wavelength of light, hindering their extensive application in light manipulation. Recently, metamaterials and metasurfaces composed of artificial nanostructures at the subwavelength scale have emerged as good candidates for achieving significant chiroptical response.[6–15] Importantly, the chiroptical response of metamaterials and metasurfaces, stemming from the optical resonance of artificial nanostructures, can be readily manipulated by adjusting their structural parameters. This flexibility opens up a myriad of possibilities for the manipulation of circularly polarized light and the study of chiroptical mechanisms, which have been successfully utilized to realize extraordinary chiroptical responses and functionalities, including chiral bound states in the continuum,[16–18] chiral exceptional

J. Cheng, Z. Li, W. Liu, Y. Zhang, S. Yu, H. Cheng, J. Tian, S. Chen
The Key Laboratory of Weak Light Nonlinear Photonics
Ministry of Education
School of Physics and TEDA Institute of Applied Physics
Nankai University
Tianjin 300071, China
E-mail: zcli@nankai.edu.cn; hcheng@nankai.edu.cn; schen@nankai.edu.cn

The ORCID identification number(s) for the author(s) of this article can be found under https://doi.org/10.1002/lpor.202401184

DOI: 10.1002/lpor.202401184

D.-Y. Choi
Laser Physics Centre
Research School of Physics
Australian National University
Canberra, ACT 2601, Australia

S. Chen
School of Materials Science and Engineering
Smart Sensing Interdisciplinary Science Center
Nankai University
Tianjin 300350, China

S. Chen
The Collaborative Innovation Center of Extreme Optics
Shanxi University
Taiyuan, Shanxi 030006, China

points,[19,20] chiral light emission,[21–23] chiral nonlinear harmonic generation,[24–26] chiral imaging, and encryption.[27,28]

The relationship between the chiroptical response of artificial nanostructures and their structural symmetry has been widely investigated to reveal the underlying chiroptical mechanisms. The chiroptical response of chiral nanostructures and their enantiomorphs has been demonstrated to always exhibit opposite characteristics, which can be continuously modulated by manipulating both their structural symmetry and parameters.[29–33] Furthermore, the modulation of coupling between different resonators has been demonstrated as a powerful alternative for achieving continuous variation of CD without sign reversal.[34–38] Recent advancements in artificial nanostructures suggest a more versatile relationship between the structural symmetry of nanostructures and their CD. The CD with opposite signs has been achieved within a fixed operational frequency band by selectively switching the local resonant mode while preserving structural symmetry. This presents a counterintuitive approach for CD sign reversal when compared to conventional methods, which typically rely on altering the structural geometric chirality to reverse the CD. For instance, the nanostructures with multiple chiral centers have been proved as good alternatives for the manipulation of the CD spectrum.[39–43] Modulating the coupling and competition of resonances within the chiral centers can result in a dramatic sign reversion of CD.[39] These achievements have significantly promoted the investigation of chiroptical nanostructures, providing new platforms for the effective manipulation of CD. However, their efficacy relies on the strategic design of chiral centers and precise manipulation of structural parameters. It is imperative to further investigate concise strategies for continuous manipulation and sign reversal of CD. Moreover, manipulation of CD in current methodologies primarily relies on controlling the resonance of nanoresonators or their coupling. The potential of modulating nonlocal resonance for versatile manipulation of CD remains relatively unexplored.

Here, we realize continuous variation and counterintuitive sign reversal of CD through controlling the collective interference of the nonlocal plasmonic guided mode resonances (GMRs) within diatomic metasurfaces, which are composed of two types of metallic nanoresonators with identical chiroptical resonant modes at adjacent resonant wavelengths. We demonstrate that the two orthogonal linearly polarized components of circularly polarized light can be effectively coupled to the same GMR. The phase difference between excited guided mode fields can be easily modulated by adjusting the spacing between nanoresonators, resulting in spin-selective constructive and destructive interference among these fields. Consequently, continuous variation and sign reversal of CD are achieved. Benefiting from the fact that the modulation of GMR does not impact the chiral resonant modes of the nanoresonators, the designed metasurfaces exhibit distinct CD at multiple wavelengths. We further experimentally demonstrate that this feature offers significant advantages in achieving spin- and wavelength-selective optical encryption. This work provides novel insights into exploring chiroptical mechanisms and holds promise for applications in chiral sensing and light spin detection.

2. Results and Discussion

The conceptual schematic depicted in **Figure 1** illustrates the continuous variation and sign reversal of CD by controlling the interference of GMRs in the diatomic metasurfaces, which have a metal-insulator-metal configuration. The thicknesses of the bottom aluminum (Al) layer, the middle SiO_2 substrate and the Al nanoresonators in the top layer are 200, 180, and 70 nm, respectively. The periods of the diatomic metasurfaces are 1200 and 600 nm in the x and y directions, respectively. The unit cell is composed of two types of nanoresonators (named A and B) with umbrella-shape, whose internal and external radii are $r_i = 160$ and $r_e = 230$ nm. The width of the middle stick is $w = 70$ nm. The angles α and β (marked in Figure 1) for the nanoresonators A and B, representing the length of the short arc and the symmetrical long arc, are $\alpha_A = \alpha_B = 45°$, $\beta_A = 80°$, and $\beta_B = 65°$. The relative spacing between nanoresonators A and B in each unit cell along the x direction is represented by d. The change in parameter d can induce a stepwise change and sign reversal of CD, which is attributed to the controllable nonlocal plasmonic GMR. The designed metasurfaces enable the efficient coupling of both transverse magnetic (TM) and transverse electric (TE) waves, which are x-polarized and y-polarized under normal incidence, into the same GMR, thereby enhancing the electric fields within the SiO_2 substrate. The interference of GMRs excited by the TM and TE components of circularly polarized waves is spin-selective due to the $\pm\pi/2$ phase delay. For simplicity, we assume that the GMRs excited by TM and TE components have equal intensity and a phase difference of $-\pi/2$. Consequently, the excited GMRs exhibit constructive and destructive interference under left-handed circularly polarized (LCP) and right-handed circularly polarized (RCP) normal illumination, respectively, amplifying the absorption of LCP waves and resulting in negative CD. Here, assuming $e^{i\omega t}$ time dependence of electromagnetic fields, RCP and LCP waves are defined such that the electric field at a fixed position z rotates in a clockwise or counterclockwise direction, respectively, when viewed from the direction toward which the wave is approaching. Crucially, changing the parameter d can effectively modulate the phase difference between the excited GMRs, enabling precise control of collective interference and CD manipulation.

To illustrate the efficacy of the designed metasurfaces in achieving continuous manipulation and counterintuitive sign reversal of CD, we initially conducted an analysis of the chiroptical response. **Figure 2**a,b depict the simulated absorption spectra at different d under LCP and RCP normal illumination. The spin-selective absorption is clearly observed at four distinct wavelengths. A high-quality absorption peak is observed at 1200 nm (P_1) under RCP illumination, while the enhanced absorption of LCP waves occurs at 1250 nm (P_2) and 1370 nm (P_3). The absorption peaks at P_1 to P_3 remain unchanged as the spacing d between two types of nanoresonators changes. However, the spin-selective absorption around 1530 nm (P_4) exhibits significant variation with different d. The absorption of RCP light is stronger than that of LCP light when the nanoresonators A and B in each unit cell are in close proximity to each other. As d gradually increases toward nearly one-half of the period, the difference between the

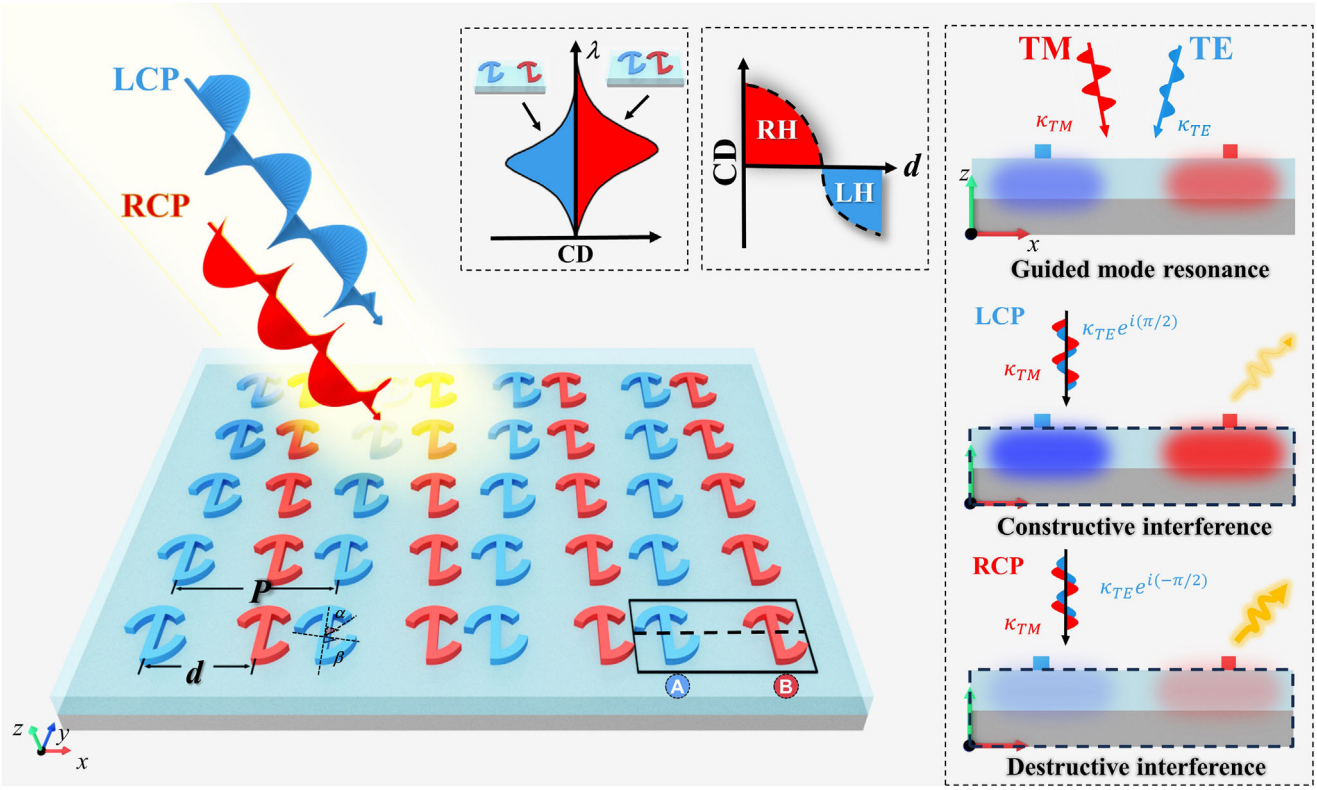

Figure 1. Schematic of the designed diatomic metasurfaces for the realization of continuous manipulation and counterintuitive sign reversal of CD. The metasurfaces are composed of two types of nanoresonators, labeled A and B, each with a distinct structural parameter β. These metasurfaces can effectively couple orthogonal linearly polarized components of circularly polarized light to the same plasmonic guided mode resonance (GMR). By adjusting the spacing parameter d, the interference of the two excited guided mode fields can be effectively manipulated, enabling continuous variation and sign reversal of CD.

absorption of LCP and RCP light decreases, and the absorption peak tends to be absent. As d further increases, the absorption of RCP light becomes weaker than that of LCP light. The changing of spin-selective absorption at P_4 indicates that the CD, defined as the absorption difference between LCP and RCP light, can be continuously manipulated by changing d, and a counterintuitive sign reversal can be observed. In addition, the CD signals are related to intrinsic planar chirality, which arises from anisotropy-induced polarization conversion (see Figure S1, Supporting Information). Furthermore, consistent with previous approaches, the mirror image of the designed metasurface exhibits opposite chiroptical responses, wherein the absorption spectra of LCP and RCP waves are exchanged.[29–33]

To elucidate the relationship between spin-selective absorption at wavelengths P_1 to P_4 and the spacing parameter d, we simulated the electric field distribution in the x-z plane across the center of the nanoresonators when $d = 500$ nm in Figure 2c. The electric field is enhanced and located in the air under RCP illumination at P_1, where a sharp peak can be observed in the absorption spectra. This behavior indicates the excitation of surface lattice resonance through the coupling of the diffracted mode to the local resonant mode, which manifests as anomalous Wood–Rayleigh absorption at the wavelength corresponding to the period size. Consequently, the chiroptical resonance at P_1 is not affected by the spacing d, but it is sensitive to the structural period along the x direction (see Figure S2, Supporting Information). The electric fields ($|E_z|$) at peaks P_2 and P_3 are enhanced near the two types of nanoresonators, indicating that P_2 and P_3 are caused by the intrinsic resonances of the two nanoresonators. We further simulated the absorption spectra of periodic metasurfaces composed of nanoresonators A and B individually (see Figure S3, Supporting Information). Results validate that the intrinsic resonances of nanoresonators A and B contribute to the absorption peaks at P_3 and P_2 respectively, which are not affected by the variation of d. The electric field is enhanced and localized within the SiO_2 substrate at P_4 under RCP illumination, with the spatial period of the field amplitude being half of the structural period along the x-direction, thereby validating the excitation of a strong plasmonic GMR.[44–46] The electric field distribution at P_4 for $d =$ 580 and 660 nm further validates that the excitation of the GMR can be modulated by varying d. At $d = 580$ nm, the GMR is excited by both LCP and RCP waves with similar resonant strengths. In contrast, at $d = 660$ nm, the GMR is effectively excited only under LCP illumination. We further experimentally validate the influence of d on the chiroptical response in Figure 2d. Four reflection peaks are evidently corresponding to the four absorption peaks. The measured reflection spectra for different d are in good agreement with the simulated ones (see Section 2, Supporting Information). The deviations in the spectra intensity and linewidth are partly due to the imperfection in sample fabrication. Moreover,

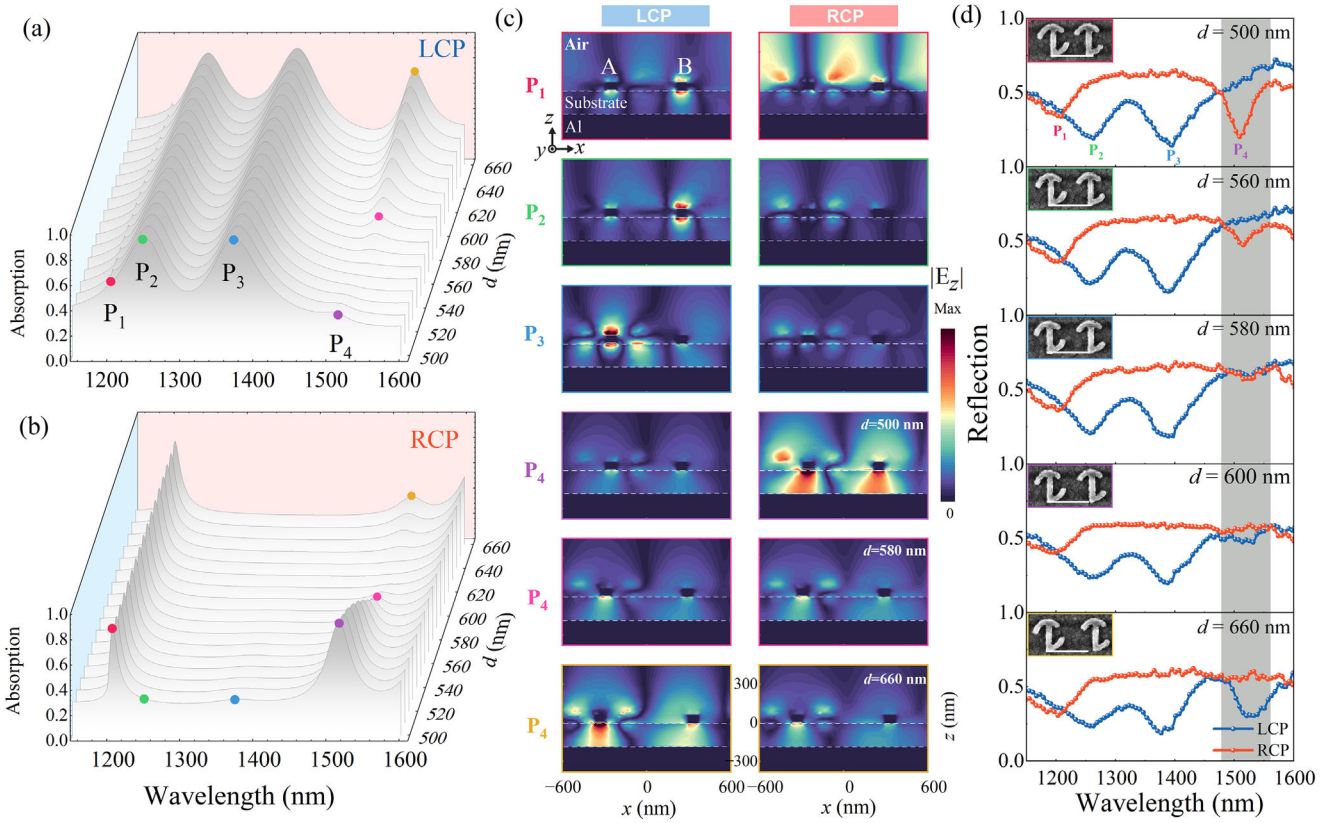

Figure 2. Analysis of the chiroptical response of the designed metasurfaces. Simulated absorption spectra of the designed metasurfaces with varying spacing d under a) LCP and b) RCP illumination. The four absorption peaks are marked as P_1 to P_4. c) Simulated amplitude distribution of z component of the electric field $|E_z|$ at the four absorption peaks in the x-z plane across the center of the two nanoresonators with $d = 500$ nm. And the simulated distribution of $|E_z|$ at P_4 under LCP and RCP illumination when $d = 580$ and 660 nm. d) Measured reflection spectra of the designed metasurfaces with different d under LCP and RCP illuminations. Insets show the SEM images of the unit cell of the designed metasurfaces (scale bar: 600 nm).

the simulation employs normal illumination conditions, while the measurement utilizes objective-focused light. This discrepancy also contributes to the observed differences between simulation and experimental results. Additionally, the low reflectivity at non-resonant wavelengths is attributed to the increased absorption losses caused by multiple reflections and optical interference within the Fabry-Pérot-like cavity formed by the metal-insulator-metal structural configuration of the designed metasurface, leading to a decrease in the overall reflectivity.

In order to quantitatively analyze the continuous variation and counterintuitive sign reversal of CD at P_4, we simulated and measured the CD spectra of the designed metasurfaces with different d in **Figure 3**a,b. Here, CD = $R_{LCP} - R_{RCP}$ (CD = $A_{RCP} - A_{LCP}$) is calculated as the difference between the reflectance of LCP and RCP light. The peak value of the simulated CD at P_4 changes from 0.55 to −0.36 with the variation of d from 500 to 660 nm, while the measured one changes from 0.37 to −0.31. The wavelength of the peak slightly redshifts as the spacing d increases. The data quality in Figure 3b is not as good as the simulated one, primarily due to the limited size of the fabricated samples (90 μm × 90 μm), which results in a weak detection signal and a reduced signal-to-noise ratio. To enhance the quality of experimental data, it would be beneficial to increase the sample size, improve the fabrication precision, and increase the power of the light source. The simulated and measured results are in reasonable agreement, validating the continuous variation and counterintuitive sign reversal of CD. These results indicate that the designed metasurface provides an effective approach for the continuous manipulation and sign reversal of CD at the resonant wavelength, without altering the structural geometric chirality. The sign reversal of CD is achieved by changing the structural geometric chirality in the most previous approaches.[29–38] Specifically, planar chiral nanostructures are defined as patterns that cannot be superimposed onto their mirror images without being lifted out of the plane. The degree of geometric chirality can be quantitatively characterized by the overlap volume between the nanostructure and its mirror image. Modifying geometric chirality involves a transformation known as "enantiomorphing", where the structure transitions from one handedness to another, passing through an achiral geometry.[47] In our design, the degree of geometric chirality remains unchanged when varying the spacing between the nanoresonators, and no enantiomorph transitions occur, thus preserving the structural geometric chirality.

This phenomenon can be attributed to the effective modulation of the spin-selective interference of the nonlocal plasmonic GMRs. The designed metasurface can effectively couple TM and TE waves into the same GMR (TM-like mode) at P_4. As the circularly polarized waves can be treated as a combination of TM

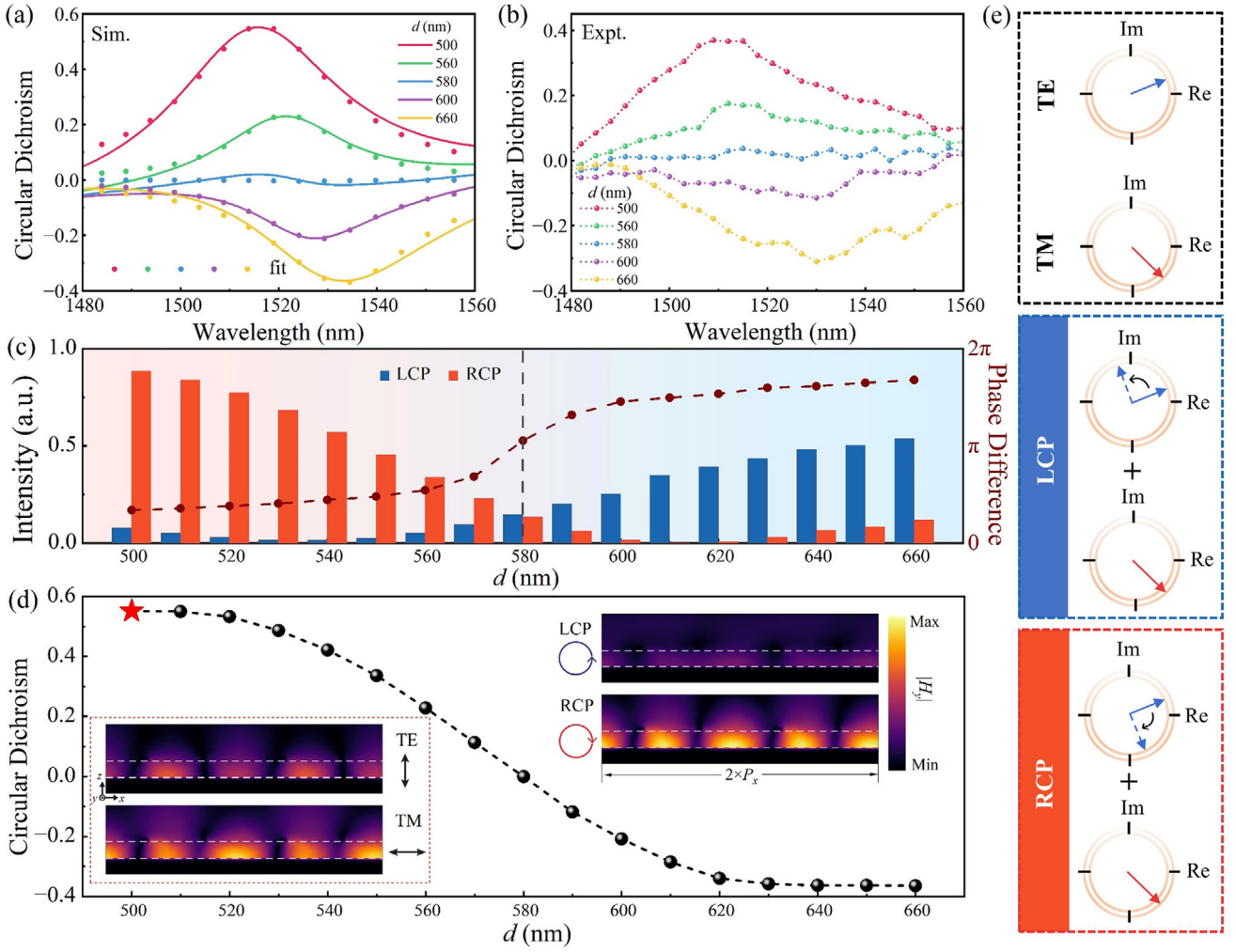

Figure 3. Continuous manipulation and counterintuitive sign reversal of CD in the designed metasurfaces by changing d. a) Simulated CD spectra of the designed metasurfaces at P_4. The dots are the theoretically fitted results based on the CMT model. b) Measured CD spectra of the designed metasurfaces. c) Calculated phase difference and corresponding normalized intensities of the interference field at P_4, and d) Simulated CD values at P_4 for different d. Insets show the simulated amplitude distribution of y component of the magnetic field distributions $|H_y|$ in the x-z plane across the center of the nanoresonators when d = 500 nm under normal illumination with various polarization state. e) The phasor representations for guided mode fields for different incident polarizations when d = 500 nm.

and TE waves with the same amplitude and a phase difference of $\pm\pi/2$, the interference between the guided mode fields excited by the TM and TE components of circularly polarized waves is spin-selective, as illustrated in Figures 3c,d. We defined the amplitude and phase of the guided mode field excited by the TM (TE) wave as a_{TM} (a_{TE}) and φ_{TM} (φ_{TE}), respectively. For LCP (RCP) light illuminating along the -z direction, the phase difference between TM and TE waves is $\pi/2$ ($-\pi/2$); therefore, the collective interference between the guided mode fields excited by TM and TE components of LCP and RCP waves can be described in terms of complex amplitude a:

$$a_{LCP} = a_{TM}e^{i\varphi_{TM}} + a_{TE}e^{i\left(\varphi_{TE}+\frac{\pi}{2}\right)} \quad (1)$$

$$a_{RCP} = a_{TM}e^{i\varphi_{TM}} + a_{TE}e^{i\left(\varphi_{TE}-\frac{\pi}{2}\right)} \quad (2)$$

Then, the intensity $I = |a|^2$ of the interference field can be obtained. The phase difference $\varphi_{TE}-\varphi_{TM}$ between the excited guided mode fields and the corresponding normalized intensities of the interference field under LCP and RCP illuminations can be calculated to show the spin-selective collective interference effect. The excited guided mode fields under TM and TE normal incidences are standing wave fields along the x axis. For the sake of simplicity, the average value of magnetic field H_y along the y axis at the crest of the standing wave field is used to calculate the phase difference. The phase difference changes in the range of 0 and π as d varies from 500 to 580 nm, as illustrated in Figure 3c. Therefore, the guided mode fields excited by TM and TE components of circularly polarized waves exhibit constructive (destructive) interference with each other under RCP (LCP) illumination, indicating the enhanced absorption of RCP light. The phase difference is close to π when d = 580 nm, and the intensities of interference fields for LCP and RCP lights are close to each other,

resulting in a weak chiroptical resonance. As d continues to increase, the phase difference is between π and 2π, which leads to constructive interference of guided mode fields for LCP light and destructive interference for RCP light. The difference in resonant strength at P_4 under LCP and RCP illuminations can be expressed as:

$$\Delta I = I_{RCP} - I_{LCP} = 4a_{TM}a_{TE}\sin\left(\varphi_{TE} - \varphi_{TM}\right) \tag{3}$$

Obviously, the sign of CD is decided by phase difference. The sin value of phase difference gradually reduces from a positive value to 0 and then changes to a negative value as d increases, which determines a continuous change in the value and sign reversal of CD. The spin-selective collective interference of guided mode fields is visually validated by the simulated magnetic field distributions in the x-z plane across the center of the nanoresonators when d = 500 nm (Figure 3d). The results validate that the proposed metasurfaces can couple both TE and TM incidence into the TM-like plasmonic GMR with similar resonant strengths. The phase difference between the excited guided mode fields leads to destructive interference under LCP illumination and constructive interference under RCP illumination, resulting in the spin-selective excitation of the GMR. The phasor representations for guided mode fields with different incident polarizations when d = 500 nm can assist in proving the interference result of the field, as shown in Figure 3e. To facilitate a quantitative comparison between the simulated results and the proposed theoretical explanation, we further employ coupled mode theory (CMT) to describe the GMR generated by the coupling of the incident wave with the metasurface.[48,49] The dynamic equations of the system can be described by:

$$\frac{da}{dt} = \left(i\omega_0 - \gamma_d - \gamma_r\right)a + \kappa_x e^{i\varphi_x}S_x + \kappa_y e^{i\varphi_y}S_y \tag{4}$$

where a, ω_0, γ_d and γ_r are the resonant amplitude, resonant frequency, dissipative loss rate, and radiative loss rate of the resonant mode. S_x (S_y) is the TM (TE) polarization component of the incident circularly polarized light. κ_x and κ_y are the coupling constants. φ_x and φ_y represent the relative phases. Based on energy conservation, $|\kappa_x|^2 + |\kappa_y|^2 = 2\gamma_r$. The LCP and RCP waves are defined as $\sqrt{\frac{1}{2}}\begin{bmatrix}1\\ i\end{bmatrix}$ and $\sqrt{\frac{1}{2}}\begin{bmatrix}1\\ -i\end{bmatrix}$. Then, the absorption of LCP and RCP waves can be expressed as:

$$A_{LCP} = \frac{2\gamma_d\left[\gamma_r - \kappa_x\kappa_y\sin\left(\varphi_y - \varphi_x\right)\right]}{\left(\omega - \omega_0\right)^2 + \left(\gamma_d + \gamma_r\right)^2} \tag{5a}$$

$$A_{RCP} = \frac{2\gamma_d\left[\gamma_r + \kappa_x\kappa_y\sin(\varphi_y - \varphi_x)\right]}{(\omega - \omega_0)2 + (\gamma_d + \gamma_r)2} \tag{5b}$$

where ω is the frequency of the optical wave. Therefore, the value of CD can be calculated as:

$$\mathrm{CD} = A_{RCP} - A_{LCP} = \frac{4\gamma_d\kappa_x\kappa_y\sin(\varphi_y - \varphi_x)}{\left(\omega - \omega_0\right)^2 + \left(\gamma_d + \gamma_r\right)^2} \tag{6}$$

According to Equation 6, the sign of CD is determined by $\Delta\varphi = \varphi_y - \varphi_x$, which is consistent with the results in Figures 3c,d. We also derive the fitted curves of the CD spectra based on Equation 6 in Figure 3a, which agree well with the simulated results. It should be noted that the negative and positive maximum values of CD occur at d equal to 500 and 660 nm, respectively. When d is less than 500 nm or greater than 660 nm, the phase difference between the guided mode fields excited by the TM and TE waves diminishes. This reduction in phase difference, in conjunction with the amplitude of the guided mode fields, leads to a decrease in the absolute value of CD. According to Equation 6, the maximum CD values can be realized by optimizing the strength of the GMRs under TE and TM illuminations to be equal, maintaining the high coupling efficiency, and keeping a phase difference of $\pm\pi/2$. The collective interference of guided mode fields is not only affected by changes in d, but also by changes in other structural parameters, for instance, β_B (see Figure S4, Supporting Information). When the relative spacing d is equal to $P_x/2$, the GMR will disappear in the metasurface composed of two identical nanoresonators (arranged as A-A or B-B). However, the GMR can be excited under both TE and TM illuminations when d is not equal to $P_x/2$. But their interference lacks spin selectivity due to the nearly constant and fixed phase difference $\Delta\varphi$ during changes in d. (Figure S5, Supporting Information). In order to realize continuous variation and counterintuitive reversal of CD at P_4, we have carefully optimized the structural parameters of the two nanoresonators in the unit cell.

In contrast to the previous approaches, our observed counterintuitive sign reversal of CD at P_4 does not originate from the chiroptical resonance of the nanoresonators or their coupling. The designed metasurfaces display distinct CD across multiple wavelengths. The effect of changing d on the chiroptical resonances at P_2 and P_3, and the surface lattice resonance at P_1 can be ignored. Taking advantage of the fact that the reflection intensity only changes with d in a narrow band spectrum at P_4, d can be used as an information-hiding perturbation. A distinctive optical encryption strategy exploiting spin states and wavelength regions as encryption channels can be obtained. Four types of unit cells with distinct d and β_A are designed as the basic elements I to IV for information coding, as shown in **Figure** 4a. The simulated reflection spectra indicate that the designed unit cells are nearly identical in the visible region and show no chiroptical resonance (Figure S8, Supporting Information). The color images of the periodic metasurfaces composed of the four types of unit cells appear almost identical (Figure 4b). The element I, composed of two nanoresonators with the same structural parameters, has no chiroptical resonance at P_3. The reflectance values of elements II, III, and IV are similar in the infrared region and are different only at P_4 under LCP illumination. Therefore, it can be expected that there are large differences in the grayscale images in the near-infrared region between periodic metasurface composed of element I and periodic metasurfaces composed of elements II to IV. And the grayscale images of periodic metasurfaces composed of elements I to IV are different at P_4. Therefore, the element I and elements II to IV can be regarded as 2-bit coding elements "1" and "0" in the near-infrared region, while they can be used to implement 4-bit light intensity encoding at P_4 under LCP illumination. On the other hand, for RCP illumination, the reflection spectra of elements II, III, and IV are almost the same in the near-infrared region and are quite different from that of element I (Figure S8, Supporting Information). Specifically, the

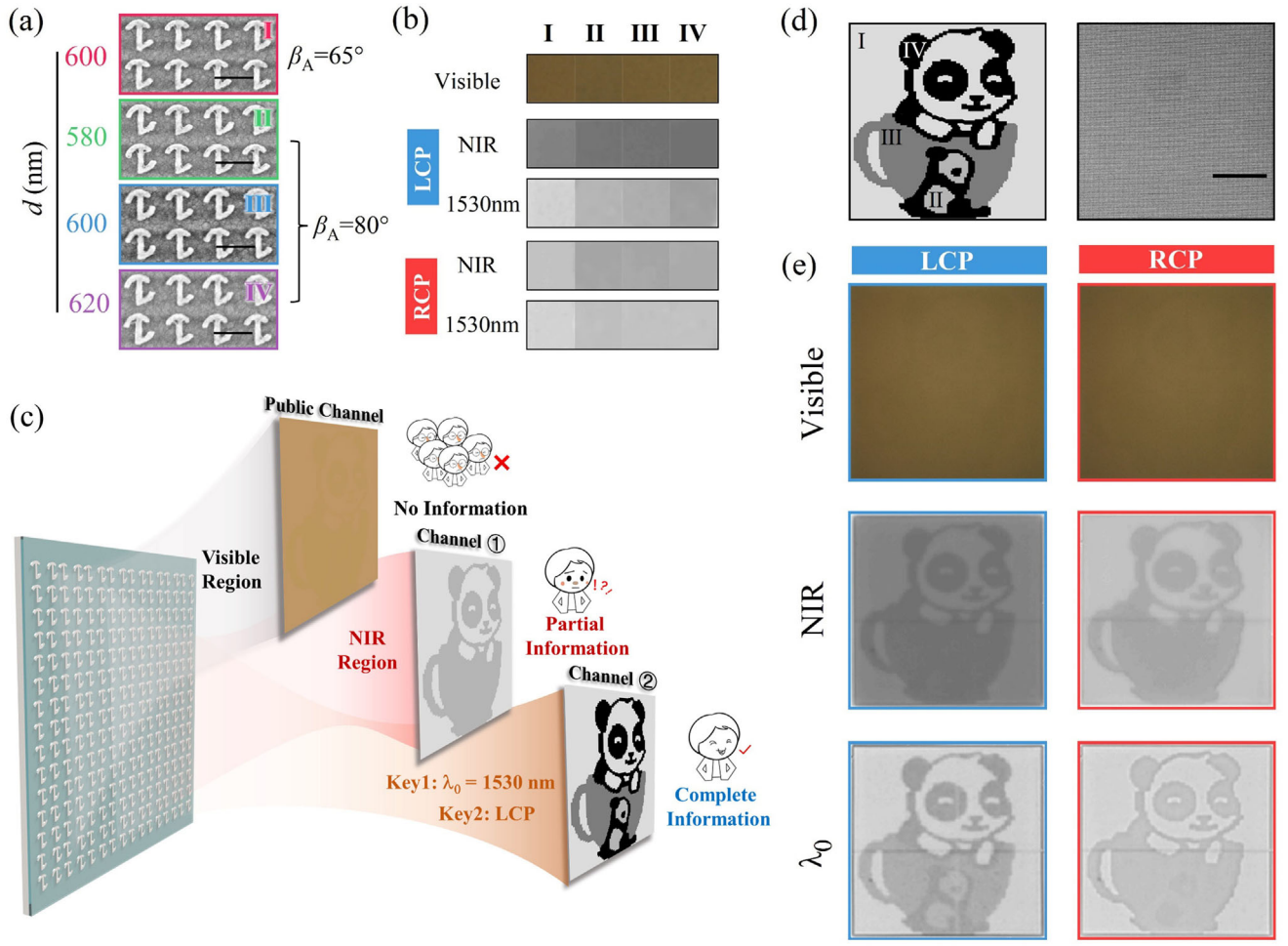

Figure 4. Realization of spin- and wavelength-selective optical encryption. a) SEM images of the designed unit cells with different β_A and d, representing four basic coding elements (I to IV). b) Measured optical images of the designed periodic metasurfaces composed of elements I to IV in the visible region, near-infrared region, and at λ_0 = 1530 nm. c) Schematic of the encryption strategy based on the designed coding elements. d) The designed encoded image and the SEM image of the fabricated sample (the scale bar is 50 μm). e) Experimentally captured optical images of the designed sample under different illumination conditions.

reflectance of the elements III and IV are identical at P_4, while that of element I is slightly higher and that of element II becomes the lowest. Therefore, the element I and elements II to IV can be regarded as 2-bit coding elements "1" and "0" in the near-infrared region to achieve the binary grayscale image under both LCP and RCP illuminations. Such results validate that spin states and wavelength regions can be used as encryption channels for chiral optical encryption. As shown in Figure 4b, the experimentally captured images of designed periodic metasurfaces validate our prediction.

To make a proof of concept, we encode two different images in the near-infrared region and at P_4, as shown in Figure 4c. The encrypted information can only be decrypted by the receiver with the correct decryption keys. If the general public has no keys, they will see no information, as the optical image is concealed with uniform intensity in the visible region. The receivers with keys will obtain partial or complete information about the image under different decryption conditions. To validate the optical encryption performance of our strategy, we encode a grayscale image into a designed metasurface in Figure 4d. The elements I to IV, representing different grayscale values, are placed in the corresponding pixels of the designed image. The image is designed with consideration of the resolution of the camera and the interactions between neighboring elements, so the areas with the same grayscale value contain at least 4 × 6 pixels. Since the nanoresonators composing the fabricated metasurface have a similar structural configuration, the encoded image cannot be observed in the overall SEM image of the fabricated sample. As validated by the experimentally captured images in Figure 4e, the fabricated metasurface appears as uniform blocks of dark orange when viewed with a visible region camera under both LCP and RCP illuminations. The infrared camera captured the binary grayscale image under both LCP and RCP illuminations from a bromine tungsten lamp. The difference in contrast between the images under LCP and RCP illuminations is attributed to the variation in the reflection spectra of each coding element under LCP and RCP illumination (see Section 3, Supporting Information). A complete and distinct panda image with four gray levels

can be observed only under LCP incidence using a narrow-band interference filter with a center wavelength of 1530 nm in front of the infrared camera. The intensity under LCP illumination follows a descending order, with the background and the face of the big panda having the highest intensity, followed by the face and belly of the small panda, then the teacup, and finally the body and eyes of both pandas. Under RCP illumination, the background and the face of the big panda still exhibit the highest intensity, while the lowest intensity is observed on the face and belly of the small panda. Additionally, the body and eye regions of the both pandas as well as the teacup appear to merge into a single intensity. The experimental results all agree well with the expected images, proving the efficiency of our strategy based on the designed metasurfaces for the realization of spin- and wavelength-selective optical encryption (as depicted in Figure 4c). In addition, since the designed metasurfaces can continuously modulate the value of CD, more elements can be further involved to encode a higher-order grayscale image at 1530 nm under LCP illumination. In contrast to previous approaches that independently encode different grayscale images into various wavelengths by controlling the local resonances of individual resonators,[32,38] the designed metasurfaces can conceal the desired grayscale image while simultaneously displaying another grayscale image under broadband illumination. This concealed image can only be revealed under narrowband illumination with a fixed circular polarization state and a specific central wavelength, offering a distinct strategy for chiral optical encryption.

3. Conclusion

In summary, we have presented an effective method for achieving continuous manipulation and counterintuitive sign reversal of CD by effectively modulating the collective interference of plasmonic GMRs in diatomic metasurfaces. By simply adjusting the relative spacing between the two types of nanoresonators, a continuous change in CD and sign reversal can be observed. We proved that tuning the spacing between the two nanoresonators induces changes in the interference phase between the guided mode fields excited by TE and TM illumination, resulting in spin-selective constructive and destructive interference between the excited guided mode fields. Experimental results validate the distinct chiral responses corresponding to different spacings between the two nanoresonators, which are in good agreement with the theoretical analysis and simulated results. Importantly, changing the spacing of nanoresonators has a negligible effect on their individual chiroptical resonances. We have experimentally proven that this feature offers significant advantages for achieving spin- and wavelength-selective optical encryption. The encoded information is confined to a narrow waveband, which is inaccessible to the general public and can be transmitted to receivers equipped with special keys. This study reveals the remarkable potential of nonlocal resonance control for manipulating the chiroptical response of nanostructures, providing a new candidate for the continuous manipulation and sign reversal of CD without changing the geometric chirality. It enhances our understanding of chiroptical mechanisms and enables applications for spin-selective light manipulation, detection, and encryption.

4. Experimental Section

Sample Fabrication: The proposed metasurfaces were fabricated by electron-beam lithography (EBL), and Al lift-off processes. A 200 nm thick Al film was initially deposited onto a microscope slide glass by using an electron-beam evaporator (Temescal BJD-2000). A 180 nm thick SiO_2 layer was subsequently deposited onto the sample by using plasma enhanced chemical vapor deposition. After that, a 200 nm thick positive electron-beam resist of ZEP520A was spin coated, and then the structure pattern was exposed using an EBL system (RAITH 150) at 30 keV. After the exposure, the sample was developed in n-amyl acetate for 60 s, rinsed with isopropyl alcohol, and then blown dry using nitrogen. A 70 nm thick Al film was subsequently deposited by using an electron-beam evaporator (Temescal BJD-2000). After the resist was removed by means of a ZEP remover (ZDMAC), the metasurfaces were created.

Numerical Simulations: The numerical simulations were performed by using the finite differential time domain methods. The optical constants of Al were taken from experimental data,[50] and the refractive index of SiO_2 was taken as 1.5. The periodic boundary conditions were set in the *x* and *y* directions to represent a periodical structure, and the waveguide port boundary was defined in the *z* direction for light incidence and reflectance. The excitation source was either a left-handed or right-handed circularly polarized plane wave.

Optical Characterizations: The experimental measurement was based on custom-built optical settings. For the experimental measurement of the reflection spectra, a bromine tungsten lamp (Zolix, GLORIA-T150A) collimated by a fiber collimator was used as the light source. The collimated beam passed through a broadband polarizer (Codixx AG, IR 1300 BC5), and an achromatic quarter-wave plate (B. Halle Nachfl, $\lambda/4$ super achromatic waveplates) to generate a circularly polarized beam. The circularly polarized beam then passed through a broadband unpolarized beam splitting prism (MFOPT, OQNP25.4N-NIR-3) and was focused on the sample with an objective (Sigma NIR plan apo 20×, NA = 0.45). The collected reflection beam passed through an achromatic quarter-wave plate (B. Halle Nachfl, $\lambda/4$ super achromatic waveplates) and a broadband polarizer (Codixx AG, IR 1300 BC5). Then the beam passed through an aperture and a lens. The focused beam then passed through a broadband unpolarized beam splitting prism (MFOPT, OQNP25.4N-NIR-3) and was collected by an optical spectrum analyzer (Zolix, Omni-750i) via a fiber coupler and an InGaAs camera (HAMAMATSU, InGaAs C10633). The data of reflection spectra were acquired with the software of the optical spectrum analyzer. In all measurements, the reflection spectra were normalized with respect to the non-nanostructure area under the same excitation conditions. The experimental setup for optical imaging at 1530 nm was modified by adding a narrow-band interference filter (Thorlabs, FB1530-12) in front of the InGaAs camera. The output light from the objective and unpolarized beam splitting prism was collected by the InGaAs camera, and the images were taken by the software of the camera. For the experimental measurement of the optical imaging in the visible region, a D65 white light (CST, CST-COPS30-W) was used as the light source. The images were captured by a CCD (TUCSEN, ISH130). Other elements in the experimental setup were replaced with visible region: polarizer (MFOPT, OPPS-25.4), quarter-wave plate (Thorlabs, AQWP05M-600), and broadband unpolarized beam splitting prism (MFOPT, OQNP25.4N-VIS).

Supporting Information

Supporting Information is available from the Wiley Online Library or from the author.

Acknowledgements

This work was supported by the National Key Research and Development Program of China (Nos. 2021YFA1400601 and 2022YFA1404501), the National Natural Science Fund for Distinguished Young Scholars (No. 11925403), the National Natural Science Foundation of China (Nos.

12122406, 12192253, 12274237, 12274239, and U22A20258), and the Natural Science Foundation of Tianjin (Nos. 22JCYBJC01350, 22JCZDJC00400 and 22JCYBJC00800).

Conflict of Interest

The authors declare no conflict of interest.

Data Availability Statement

The data that support the findings of this study are available from the corresponding author upon reasonable request.

Keywords

chiral metasurface, circular dichroism, optical collective interference, perturbative encryption, plasmonic guided mode resonance

Received: July 28, 2024
Revised: October 25, 2024
Published online:

[1] D. P. Glavin, A. S. Burton, J. E. Elsila, J. C. Aponte, J. P. Dworkin, *Chem. Rev.* **2020**, *120*, 4660.
[2] G. Wang, H. Zhang, H. Kuang, C. Xu, L. Xu, *Matter* **2023**, *6*, 1752.
[3] Y. Chen, W. Du, Q. Zhang, O. Ávalos-Ovando, J. Wu, Q.-H. Xu, N. Liu, H. Okamoto, A. O. Govorov, Q. Xiong, C.-W. Qiu, *Nat. Rev. Phys.* **2021**, *4*, 113.
[4] M. Liu, L. Zhang, T. Wang, *Chem. Rev.* **2015**, *115*, 7304.
[5] A. Lininger, G. Palermo, A. Guglielmelli, G. Nicoletta, M. Goel, M. Hinczewski, G. Strangi, *Adv. Mater.* **2023**, *35*, 2107325.
[6] M. Hentschel, M. Schäferling, X. Duan, H. Giessen, N. Liu, *Sci. Adv.* **2017**, *3*, e1602735.
[7] J. K. Gansel, M. Thiel, M. S. Rill, M. Decker, K. Bade, V. Saile, G. Von Freymann, S. Linden, M. Wegener, *Science* **2009**, *325*, 1513.
[8] Y. Zhao, M. A. Belkin, A. Alù, *Nat. Commun.* **2012**, *3*, 870.
[9] F. Zhang, M. Pu, X. Li, P. Gao, X. Ma, J. Luo, H. Yu, X. Luo, *Adv. Funct. Mater.* **2017**, *27*, 1704295.
[10] C. Wang, Z. Li, R. Pan, W. Liu, H. Cheng, J. Li, W. Zhou, J. Tian, S. Chen, *ACS Photonics* **2020**, *7*, 3415.
[11] L. Mao, K. Liu, S. Zhang, T. Cao, *ACS Photonics* **2020**, *7*, 375.
[12] Y. Huang, T. Xiao, Z. Xie, J. Zheng, Y. Su, W. Chen, K. Liu, M. Tang, J. Zhu, P. Müller-Buschbaum, L. Li, *ACS Appl. Mater. Interfaces* **2021**, *13*, 45890.
[13] Z. Wang, L. Jing, K. Yao, Y. Yang, B. Zheng, C. M. Soukoulis, H. Chen, Y. Liu, *Adv. Mater.* **2017**, *29*, 1700412.
[14] J. Qin, L. Deng, T. Kang, L. Nie, H. Feng, H. Wang, R. Yang, X. Liang, T. Tang, J. Shen, C. Li, H. Wang, Y. Luo, G. Armelles, L. Bi, *ACS Nano* **2020**, *14*, 2808.
[15] Z. Han, F. Wang, J. Sun, X. Wang, Z. Tang, *Adv. Opt. Mater.* **2023**, *11*, 2301022.
[16] M. V. Gorkunov, A. A. Antonov, Y. S. Kivshar, *Phys. Rev. Lett.* **2020**, *125*, 093903.
[17] T. Shi, Z.-L. Deng, G. Geng, X. Zeng, Y. Zeng, G. Hu, A. Overvig, J. Li, C.-W. Qiu, A. Alù, Y. S. Kivshar, X. Li, *Nat. Commun.* **2022**, *13*, 4111.
[18] Y. Chen, H. Deng, X. Sha, W. Chen, R. Wang, Y.-H. Chen, D. Wu, J. Chu, Y. S. Kivshar, S. Xiao, C.-W. Qiu, *Nature* **2023**, *613*, 474.
[19] M. Kang, J. Chen, Y. D. Chong, *Phys. Rev. A* **2016**, *94*, 033834.
[20] Q. Song, M. Odeh, J. Zúñiga-Pérez, B. Kanté, P. Genevet, *Science* **2021**, *373*, 1133.
[21] X. Zhang, Y. Liu, J. Han, Y. Kivshar, Q. Song, *Science* **2022**, *377*, 1215.
[22] S. Wang, W. Qin, S. Zhang, Y. Lou, C. Liu, T. Wu, Q. He, C. Tian, L. Zhou, Y. Wu, Z. Tao, *Nano Lett.* **2022**, *22*, 10111.
[23] A. Nguyen, J.-P. Hugonin, A.-L. Coutrot, E. Garcia-Caurel, B. Vest, J.-J. Greffet, *Optica* **2023**, *10*, 232.
[24] L. Kang, S. P. Rodrigues, M. Taghinejad, S. Lan, K.-T. Lee, Y. Liu, D. H. Werner, A. Urbas, W. Cai, *Nano Lett.* **2017**, *17*, 7102.
[25] Y. Jiang, W. Liu, Z. Li, D. Choi, Y. Zhang, H. Cheng, J. Tian, S. Chen, *Adv. Opt. Mater.* **2023**, *11*, 2202186.
[26] K. Koshelev, Y. Tang, Z. Hu, I. I. Kravchenko, G. Li, Y. Kivshar, *ACS Photonics* **2023**, *10*, 298.
[27] Y. Chen, J. Gao, X. Yang, *Adv. Opt. Mater.* **2019**, *7*, 1801467.
[28] H. Wang, Z. Qin, H. Zhou, C. Li, H. Bai, X. Li, Y. Li, J. Zhang, S. Qu, L. Huang, *Laser Photonics Rev.* **2023**, *17*, 2200545.
[29] M. Hentschel, M. Schäferling, T. Weiss, N. Liu, H. Giessen, *Nano Lett.* **2012**, *12*, 2542.
[30] W. Li, Z. J. Coppens, L. V. Besteiro, W. Wang, A. O. Govorov, J. Valentine, *Nat. Commun.* **2015**, *6*, 8379.
[31] Q. Wang, E. Plum, Q. Yang, X. Zhang, Q. Xu, Y. Xu, J. Han, W. Zhang, *Light Sci. Appl.* **2018**, *7*, 25.
[32] Z. Li, W. Liu, H. Cheng, D. Choi, S. Chen, J. Tian, *Adv. Mater.* **2020**, *32*, 1907983.
[33] Z. Shen, S. Fan, W. Yin, S. Li, Y. Xu, L. Zhang, X. Chen, *Laser Photonics Rev.* **2022**, *16*, 2200370.
[34] X. Yin, M. Schäferling, B. Metzger, H. Giessen, *Nano Lett.* **2013**, *13*, 6238.
[35] W. Zhang, B. Ai, P. Gu, Y. Guan, Z. Wang, Z. Xiao, G. Zhang, *ACS Nano* **2021**, *15*, 17657.
[36] S. Yin, Y. Chen, B. Quan, S. Liu, W. Huang, M. Liu, W. Zhang, J. Han, *Nanophotonics* **2023**, *12*, 1317.
[37] Y. Tang, Y. Liang, J. Yao, M. K. Chen, S. Lin, Z. Wang, J. Zhang, X. G. Huang, C. Yu, D. P. Tsai, *Laser Photonics Rev.* **2023**, *17*, 2200597.
[38] J. Cheng, Z. Li, D. Choi, S. Yu, W. Liu, H. Wang, Y. Zhang, H. Cheng, J. Tian, S. Chen, *Adv. Opt. Mater.* **2023**, *11*, 2202329.
[39] C.-Y. Ji, S. Chen, Y. Han, X. Liu, J. Liu, J. Li, Y. Yao, *Nano Lett.* **2021**, *21*, 6828.
[40] X. Li, C. Ji, S. Chen, Y. Han, J. Liu, J. Li, *Adv. Opt. Mater.* **2021**, *9*, 2101191.
[41] S. Chen, C.-Y. Ji, Y. Han, X. Liu, Y. Wang, J. Liu, J. Li, *APL Photonics* **2022**, *7*, 056102.
[42] W. Wei, S. Chen, C. Ji, S. Qiao, H. Guo, S. Feng, J. Li, *Opt. Express* **2021**, *29*, 33572.
[43] X. Sun, J. Yang, L. Sun, G. Yang, C. Liu, Y. Tao, Q. Cheng, C. Wang, H. Xu, Q. Zhang, *ACS Nano* **2022**, *16*, 19174.
[44] S. A. Safiabadi Tali, W. Zhou, *Nanophotonics* **2019**, *8*, 1199.
[45] B. Wang, P. Yu, W. Wang, X. Zhang, H. C. Kuo, H. Xu, Z. M. Wang, *Adv. Opt. Mater.* **2021**, *9*, 2001520.
[46] W. Zhou, J. Y. Suh, Y. Hua, T. W. Odom, *J. Phys. Chem. C* **2013**, *117*, 2541.
[47] J. T. Collins, X. Zheng, N. V. S. Braz, E. Slenders, S. Zu, G. A. E. Vandenbosch, V. V. Moshchalkov, Z. Fang, M. Ameloot, P. A. Warburton, V. K. Valev, *Advanced Opt. Mater.* **2018**, *6*, 1800153.
[48] S. Fan, W. Suh, J. D. Joannopoulos, *J. Opt. Soc. Am. A* **2003**, *20*, 569.
[49] X. Guo, C. Liu, H. C. Ong, *Phys. Rev. Appl.* **2021**, *15*, 024048.
[50] M. R. Querry, *US Army Chem. Res. Dev. Eng. Cent. CRDC Aberd. Proving Ground MD* **1985**, *418*.

